Single and Dual-Doppler Radar Observations of a Nontornadic Supercell Thunderstorm on 6 June 2010

Zachary Wienhoff, Manda Chasteen, and Jeffrey Frame
Department of Atmospheric Sciences, University of Illinois at Urbana-Champaign, Urbana, IL

1. Introduction

Two Doppler on Wheels (DOW) radars (Wurman et al. 1997) intercepted a nontornadic supercell near Ogallala, Nebraska, on 6 June 2010 during the Verification of the Origins of Rotation in Tornadoes Experiment 2 (VORTEX2; Wurman et al. 2012). This storm initiated within a disorganized cluster of convection north of Sidney, Nebraska, at approximately 2000 UTC in a region of moist upslope flow east of a lee surface trough (Fig. 1a). The 0-6 km bulk shear was greater than 60 knots (Fig. 1b), which was more than sufficient for organized convection, including supercells. As the storm progressed eastward and the low-level shear strengthened, the storm entered a region with 0-1 km storm-relative helicity (SRH) of approximately 200 m^2 s^{-2} (Fig. 1c). Within this regime, the easternmost cell organized into a right-moving supercell at around 2200 UTC.

Mobile Doppler radar observations began at approximately 2245 UTC, while the storm was a mature supercell, and lasted for approximately 90 minutes, by which time the storm had weakened significantly. Only twelve minutes of dual-Doppler data were available for analysis, however, owing to the radars moving to keep up with the storm.

This supercell is of interest because the close proximity of the radars to the storm (less than 15 km) allows for relatively high-resolution objective analyses of radar reflectivity, radial velocity, vertical vorticity, and the three-dimensional wind field near the mesocyclone. While detailed analyses of one of the strong tornadoes intercepted by VORTEX2 have been published (e.g., Wakimoto et al. 2011; Markowski et al. 2012a, b; Atkins et al. 2012; Kosiba et al. 2013), detailed examinations of nontornadic supercells (e.g., Trapp 1999; Wakimoto and Kai 2000; Beck et al. 2006; Frame et al. 2009) are equally important in determining potentially significant differences between tornadic and nontornadic supercells.

The primary focus of this paper is to document the temporal evolution of the rear-flank downdraft (RFD), rear-flank gust front, and mesocyclone, and to draw preliminary conclusions as to why the storm failed to produce a tornado during the time in which it was observed by the radars. A brief overview of the data and methodology can be found in section 2. Section 3 presents the radar observations, and preliminary conclusions and future work are listed in section 4.

2. Data and Methodology

Data from two mobile Doppler radars (DOW6 and DOW7) are presented after being edited for quality using SoloII software (Oye et al. 1995). These radars were initially located approximately 25 km south of Ogallala, NE, before relocating southeast to follow the supercell (Fig. 2). Both DOW radars are dual-polarization, X-band (3.2 cm wavelength) radars and have a beamwidth of 0.95°. Volume scans were completed simultaneously every two minutes and included elevation angles of 0.5°, 1°, 2°, 3°, 4°, 5°, 6°, 8°, 10°, 12°, and 14°. Quality control included removing data with poor signal-to-noise ratios, deleting second trip echoes, and dealiasing folded velocities. These data were then mapped to a Cartesian grid using

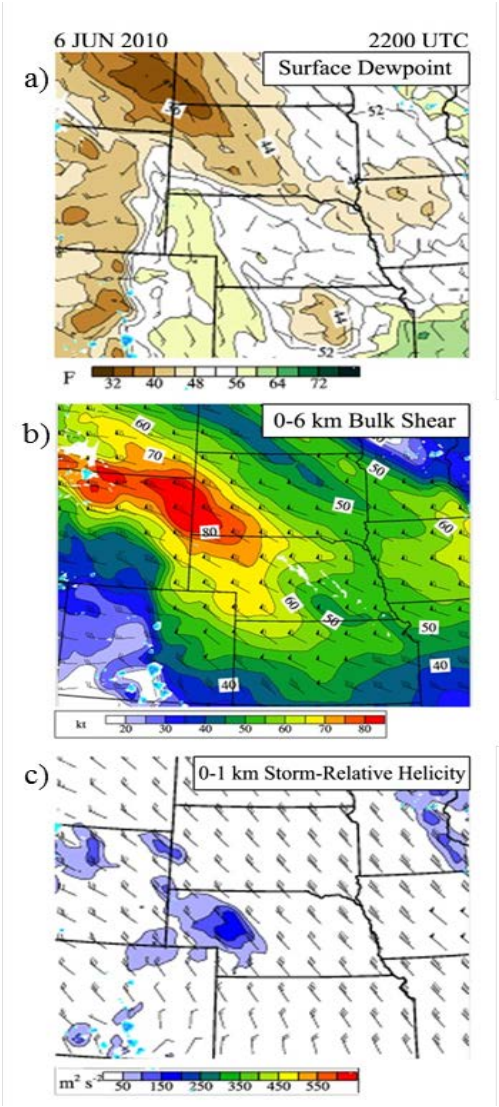

Fig 1. 22-hour NSSL WRF forecast initialized at 0000 UTC 6 June 2010 for the northern Great Plains. Included products are (a) surface dewpoint temperatures (°F) and wind barbs (knots), (b) 0-6 km bulk shear (knots), (c) 0-1 km storm-relative helicity (SRH; $m^2 s^{-2}$).

Observation Processing And Wind Synthesis (OPAWS) software and a two-pass Barnes analysis (Barnes 1964). For both the single and dual-Doppler analyses, the grid spacing in the *x*, *y*, and *z* directions is 0.2 x 0.2 x 0.1 km, respectively. A smoothing parameter of κ = 0.419 km^2 was used for the objective analyses ran for the dual-Doppler analyses, and a smoothing parameter of κ = 0.720 km^2 was used for the single-Doppler objective analyses (Koch et al. 1983). These smoothing factors were multiplied by constant factor γ = 0.3 for the second pass of the Barnes analyses (Majcen et al 2008). The top of the dual-Doppler domain was set at 1.5 km AGL. The above objective analysis parameters are consistent with the recommendations given by Pauley and Wu (1990) and Marquis et al. (2007).

Thermodynamic data were obtained by mobile mesonets, which collected data of temperature, dewpoint temperature, pressure, and wind speed and direction at 3 m AGL (Straka et al. 1996). The thermodynamics of the environmental inflow were characterized by time-weighted observations from the automated surface observing system (ASOS) located in Imperial, Nebraska, at 2253, 2322, 2339, and 2353 UTC.[1] Mobile mesonet data included in the analyses were collected during a 10-minute interval centered on the radar observation time. These data were used to derive virtual potential temperature perturbations (θ_v') and equivalent potential temperature perturbations (θ_e') by subtracting the mean state from the mesonet observations. Thermodynamic parameters such as θ_v' and θ_e' can indicate the potential buoyancy within the RFD and hence the potential for violent, long-tracked tornadoes (e.g., Markowski et al. 2002).[2]

3. Observations

When the mobile-Doppler radar observations began at 2246 UTC, the storm had developed a hook echo and displayed a "flying eagle" signature, with a V-shaped notch within the forward-flank reflectivity core (e.g., van den

[1] The ASOS sites located closer to the supercell were not representative of the inflow environment. Ogallala, Nebraska, was located in the outflow of the supercell, and McCook, Nebraska, was affected by anvil shading (Frame and Markowski 2013).

[2] Markowski et al. 2002 found that smaller deficits of θ_v' and θ_e' were found in RFDs of tornadic supercells, whereas nontornadic supercells were characterized of potentially colder RFDs.

Broeke et al. 2008; Kumjian and Schenkman 2008; Frame et al. 2009). The storm motion was toward the SSE at 8 m s^{-1} at this time. The maximum reflectivity within the core was approximately 75 dBZ per WSR-88D imagery (Figs. 3a and 3b). The storm began to lose organization around 2339 UTC (Fig. 3c), and reflectivity values within the core began to decrease. The storm motion increased to 17 m s^{-1} toward the ESE near the end of the observation period. After this time, VORTEX2 abandoned this storm in favor of another storm farther to the north, which is not discussed herein.

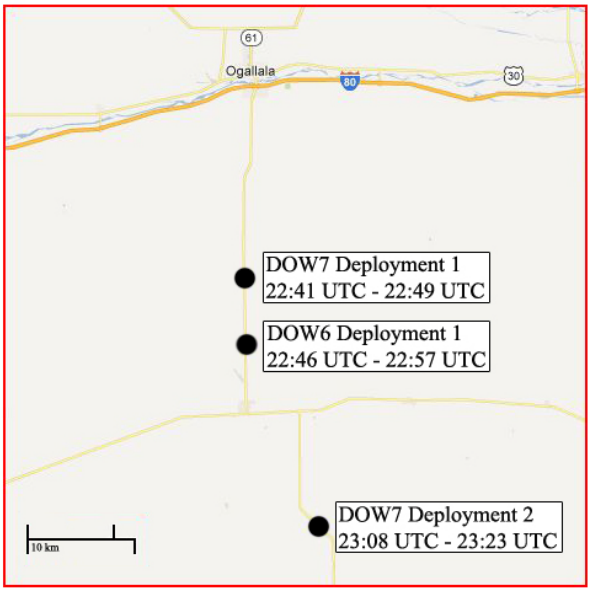

Fig 2. Map of the DOW deployment sites. Corresponding observation times are shown.

At the beginning of the mobile radar observation period, east-southeasterly winds ranging from 8 to 16 m s^{-1} existed within the storm inflow southeast of the cell and persisted throughout the scanning period. A prominent hook echo is visible in the first volume scan from DOW7 (not shown) at 2246 UTC. In the DOW data, the storm displayed a maximum reflectivity around 55 dBZ near the hook echo. The left-forward flank of the storm is not visible on DOW imagery because of beam attenuation in the heavy rain and hail within the forward flank.[3]

A line of enhanced reflectivity values extending from the forward flank precipitation core about 5 km west of the first DOW7 deployment site and arcing southwestward, marks the rear-flank gust front (Figs. 4a and 5a). Low-level convergence is visible along this feature (Fig. 4).

Upward vertical velocities exceeding 10 m s^{-1} at 1 km AGL are present within the primary updraft east of the hook echo (Fig. 6a). Downward vertical velocities exceeding -10 m s^{-1} near the hook echo are indicative of subsidence within the RFD (Fig. 6b).

A dual-Doppler wind synthesis from 2246 UTC reveals that the mesocyclone at 100 m above ground level (AGL) was located at the tip of the inflow notch near the updraft/downdraft interface. This vortex is strongest at 100 m, as shown in the vertical vorticity field (Fig. 5a), and extends vertically to an altitude of 1.2 km AGL (note that this vortex is weaker at 1.0 km AGL in Fig. 5b). The rear-flank gust front wraps into the mesocyclone at 100 m AGL (Fig. 5a). The outflow behind this gust front is approximately 800 m deep (compare the winds in Figs. 5a and 5b). At 1 km AGL, another circulation is evident near the tip of the hook echo (Fig. 5b), which strengthens with height to the top of the dual-Doppler domain at 1.5 km AGL (not shown). Below 800 m, this circulation is weak because it is located within a region of divergent outflow.

Photographs taken by one of the authors at 2243 and 2245 UTC (Figs. 7a and 7b) of the updraft base provide a visualization of the positive and negative vertical velocities seen in the 2246 UTC dual-Doppler analyses. Between 2243 and 2245 UTC, the wall cloud and low-level mesocyclone become tilted as a

[3] The 3-cm wavelength beam used by the DOW radars experiences significantly more attenuation as compared to the 10-cm wavelength used by the WSR-88D radars (Doviak and Zrnic 1993, p. 42).

surge of outflow from the north (from the right of Figs. 7a and 7b) undercuts the circulation. This surge of outflow is coincident with negative vertical velocities in Fig. 6b.

The thermodynamic analyses valid at 2246 UTC illustrate that the inflow region is characterized by a θ_v value of approximately 310 K (Fig. 4a), and θ_e values ranging from 345 – 346 K (Fig. 4b). No mobile mesonet data exist within the RFD at this time. The mobile mesonets winds indicate easterly surface flow of approximately 5 m s^{-1} in the inflow region. These observations were along the baseline of the dual-Doppler lobes, which could account for discrepancies with the dual-Doppler wind field. Additionally, increased friction at 3 m AGL could account for lower wind speeds and increased backing when compared to the dual-Doppler derived winds at approximately 100 m AGL. Inflow approximately parallel to the forward-flank gust front provides streamwise baroclinically-generated horizontal vorticity, which is then advected toward and tilted vertically by the updraft, forming the low-level mesocyclone seen in Fig. 5a (e.g., Rotunno and Klemp 1985).

Both DOW6 and DOW7 relocated southeastward to follow the storm, so no dual-Doppler data exist after 2246 UTC. By 2309 UTC, DOW7 was located at its second deployment site, roughly 25 km SSE of its first deployment location (Fig. 2). At 2309 UTC, the reflectivity core and hook echo were largely unchanged from earlier (compare Figs. 4a and 8a). Additional convection formed to the rear of the storm and is visible as the band of high reflectivity values extending northwestward from the hook echo (Fig. 8a). A fine line of enhanced reflectivity values marks the location of the rear-flank gust front approximately 3 km west and 8 km north of the radar site; it is oriented nearly parallel to, but about 5 km east of the hook echo.[4] The gust front has moved farther from the hook echo since 2246 UTC (compare Figs. 4a and 8a).

A velocity couplet at 100 m AGL was not evident near the hook echo from the single-Doppler radial velocity data at this time. It is likely that the shallow circulation seen in the 2246 UTC analysis (Fig. 5a) was unable to persist within the surging divergent outflow. Owing to a strengthening cold pool, the rear-flank gust front accelerated southeastward and reached speeds of 12 to 16 m s^{-1} (compare Figs. 5a and 8a).

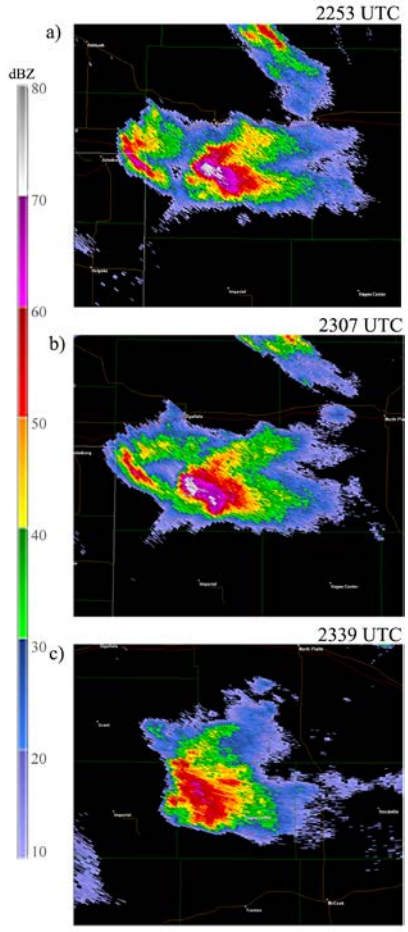

Fig 3. KLNX WSR-88D radar reflectivity at (a) 2253 UTC, (b) 2307 UTC, and (c) 2339 UTC 6 June 2010.

[4] The apparent break in the gust front approximately 4 km west and 6 km north of the radar site is caused by beam blockage owing to several buildings and large trees northwest of the radar location.

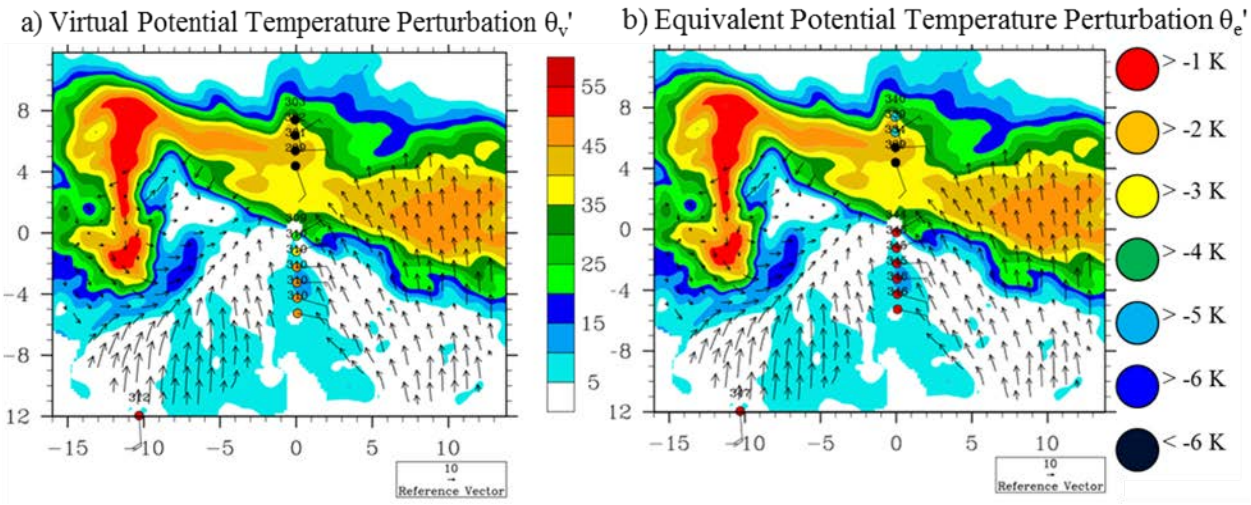

Fig. 4. Radar reflectivity and dual-Doppler wind field at 100 m AGL at 2246 UTC overlaid with mobile mesonet winds at 3 m AGL, (a) virtual potential temperature perturbation, and (b) equivalent potential temperature perturbation data valid at 2246 UTC 6 June 2010.

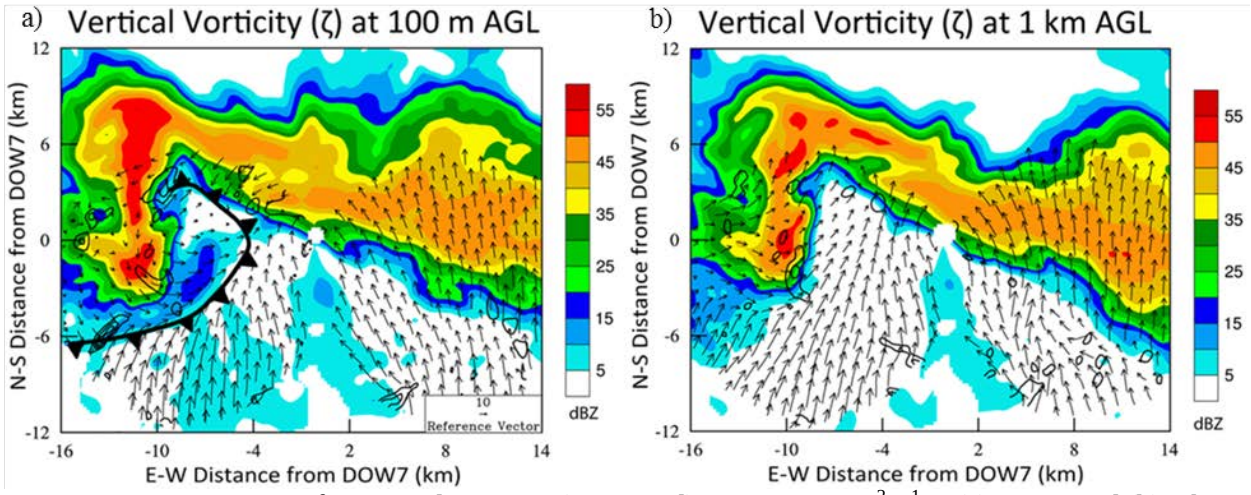

Fig. 5. As in Fig. 4 except for vertical vorticity (contoured) every 1.5 x 10^{-2} s^{-1} at (a) 100 m and (b) 1 km AGL. The rear-flank gust front is indicated by the cold front in (a).

The thermodynamic analysis valid at 2309 UTC indicates the inflow region to be approximately unchanged from 2246 UTC, with θ_v values of 310 – 311 K (Fig. 8a) and θ_e values of 344 – 346 K (Fig. 8b). Thermodynamic data near the tip of the hook echo show θ_v values of 304 – 305 K (Fig. 8a), and θ_e values of 342 – 343 K (Fig. 8b). Virtual potential temperature deficits of more than 6 K exist in the outflow region, while θ_e deficits are approximately 1 – 3 K in this region. These data indicate that little to no surface-based convective available potential energy (CAPE) was likely present within the rear-flank downdraft (or that any such CAPE was strongly capped) which is a necessary condition for tornadogenesis (Markowski et al. 2002). However, no mesonet data exist within the RFD outside of the precipitation region at this time.

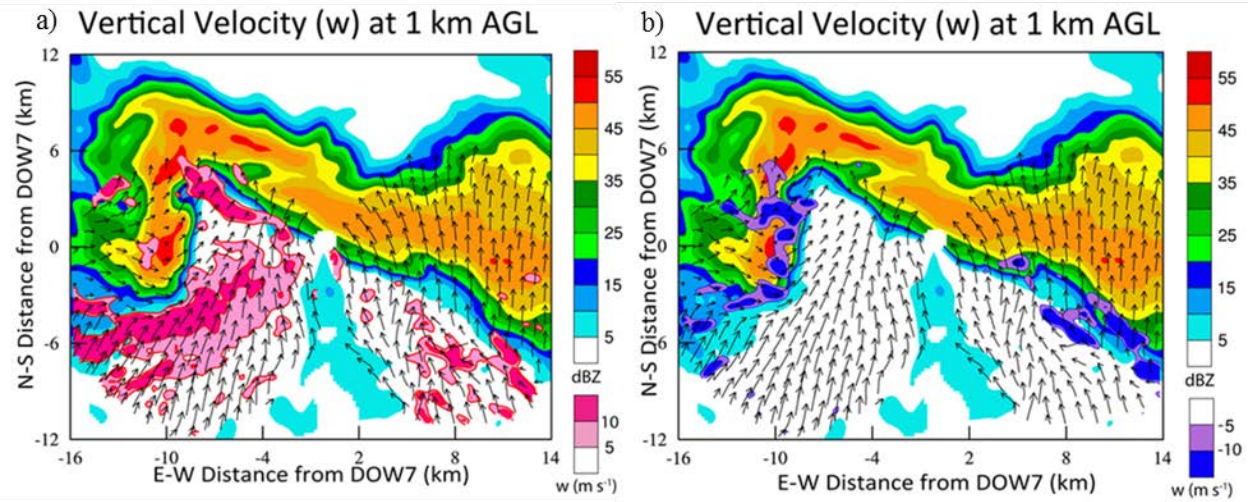

Fig. 6. Radar reflectivity, dual-Doppler wind field at 1 km AGL, (a) updraft velocity at 1 km AGL, and (b) downdraft velocity at 1 km AGL (shaded every 5 m s^{-1} as indicated) at 2246 UTC 6 June 2010.

By 2319 UTC, the storm began to weaken significantly. Reflectivity values within the hook echo and most of the precipitation core decreased to less than 50 dBZ (Fig. 9a). The hook echo also began to lose organization as seen by the lack of an enhanced ball-like reflectivity signature near its southern tip. The rear-flank gust front continued to surge southeast at speeds in excess of 12 m s^{-1}, segregating the updraft from buoyant environmental inflow (compare Figs. 8b and 9b).

Whereas the wind shift at the gust front at 2309 UTC was less evident (Fig. 8b), the 2319 UTC volume scan depicts a distinct wind shift at the gust front (Fig. 9b). Outbound velocities near 20 m s^{-1} behind the gust front converge with inbound velocities of approximately 16 m s^{-1} in the inflow region.

The thermodynamic analysis valid at 2319 UTC depicts that the inflow region is characterized by θ_v values around 312 K. Within the RFD, θ_v values range from approximately 304 - 305 K just north of the boundary to approximately 304 K farther into downdraft region (Fig. 9a). This yields θ_v deficits in the outflow in excess of 6 K. The inflow region is characterized by θ_e values of approximately 345 K, with deficits of 3 - 4 K in the RFD (Fig. 9b).

As the advancing cold pool progressed farther southeast, the updraft became increasingly removed from the potentially warm, moist inflow, forcing the storm to continue to weaken. At this time, the DOW radars continued to follow the storm, but as the storm weakened further, they abandoned this storm in favor of another cell to the north.

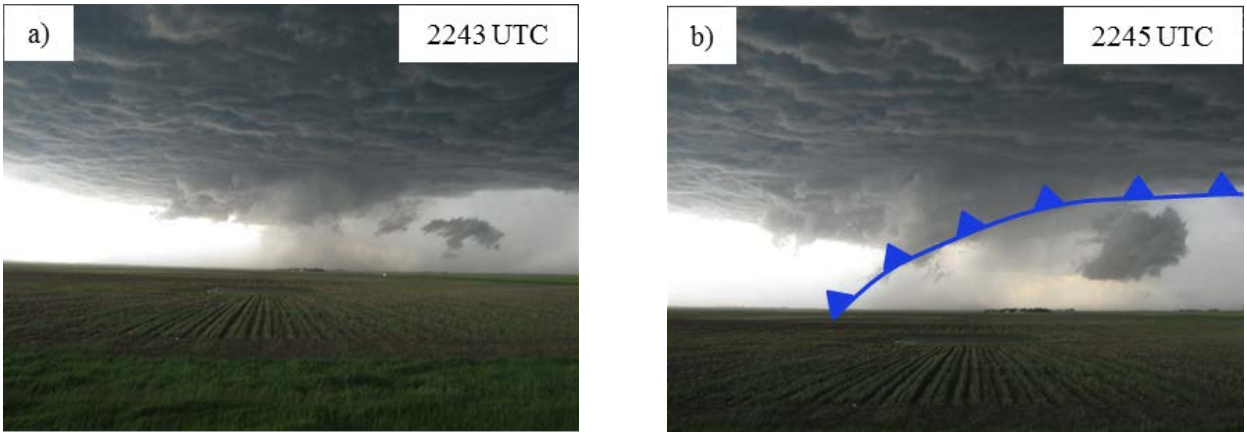

Fig 7. Photographs taken from the location of DOW7 looking west toward the updraft region of the supercell at (a) 2243 UTC and (b) 2245 UTC 6 June 2010. The blue cold front in (b) shows the approximate position of the rear-flank gust front.

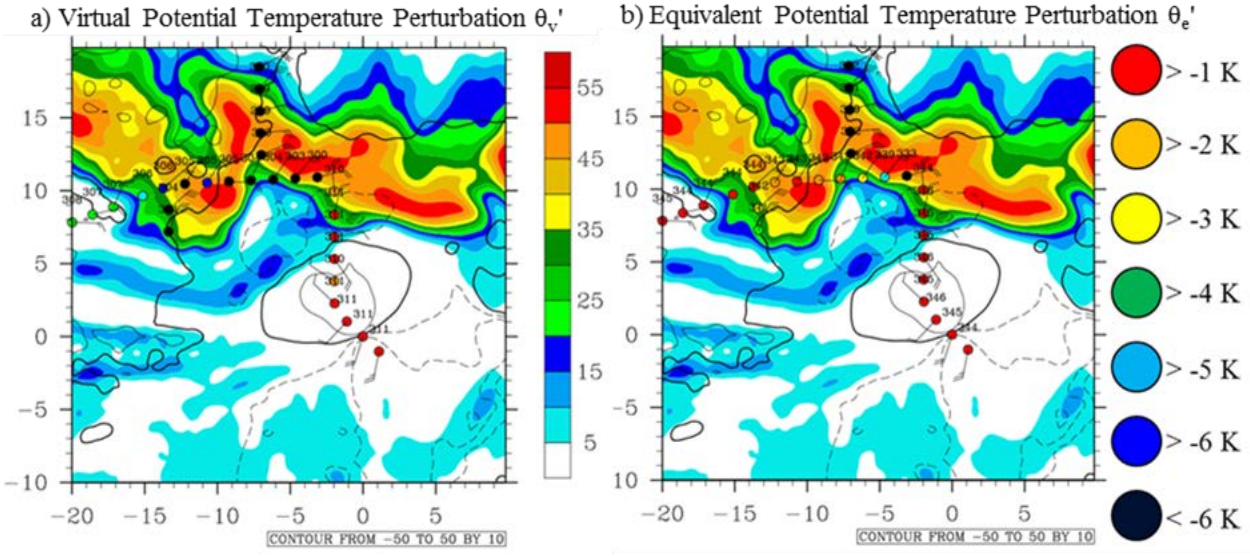

Fig. 8. Radar reflectivity, radial velocity (contoured; thick black contour represents 0 m s^{-1}, dashed contours represent inbound velocities, and solid contours represent outbound velocities), mobile mesonet winds at 3 m AGL, (a) virtual potential temperature perturbation, and (b) equivalent potential temperature perturbation at 2309 UTC 6 June 2010.

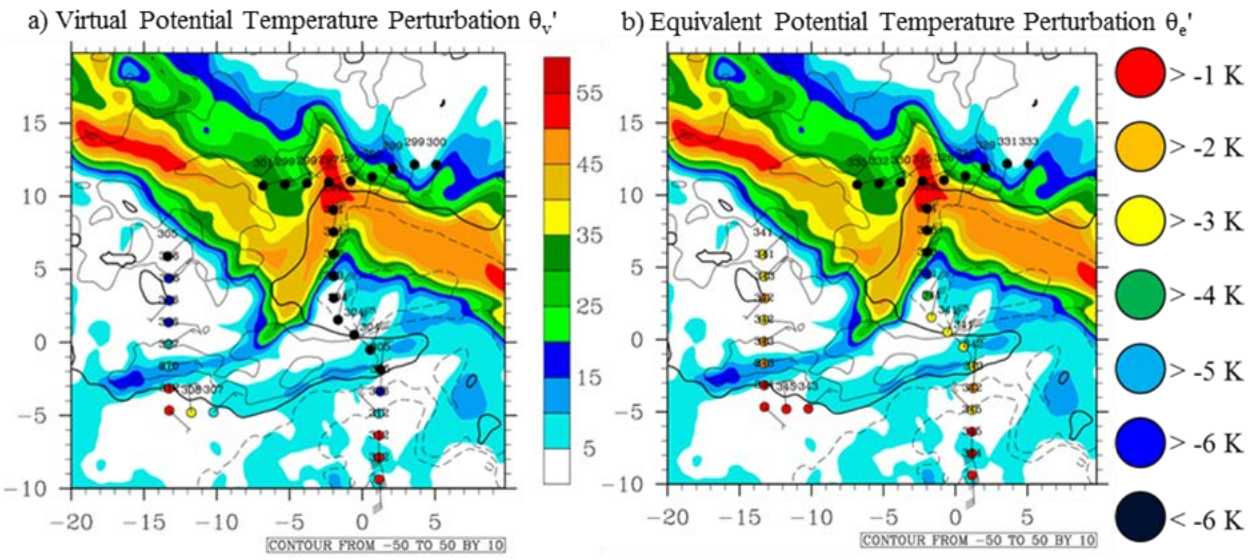

Fig. 9. Radar reflectivity, radial velocity (contoured; thick black contour represents 0 m s^{-1}, dashed contours represent inbound velocities, and solid contours represent outbound velocities), mobile mesonet winds at 3 m AGL, (a) virtual potential temperature perturbation, and (b) equivalent potential temperature perturbation at 2319 UTC 6 June 2010.

4. Conclusions

The Doppler radar analyses of this nontornadic supercell presented herein indicate that this storm, which was initially a mature supercell with a low-level mesocyclone, weakened as the rear-flank gust front advanced several kilometers ahead of the hook echo and updraft. The surging cold pool deprived the supercell updraft of the buoyant environmental inflow necessary for storm sustenance. Thus, the potentially cold temperatures of the rear-flank downdraft inhibited tornadogenesis and eventually led to the demise of the supercell.

Thermodynamic data valid when the storm was a mature, right-moving supercell indicate that the negatively buoyant, potentially cold rear-flank downdraft prohibited the reingestion of these parcels by the updraft. Thus, vortex intensification via stretching was inhibited, and this storm failed to produce a tornado.

Acknowledgements. We want to thank all of the VORTEX2 volunteers (too numerous to mention) who helped with the collection of data. We also wish to thank David Wojtowicz and Dr. Ken Patten of the Department of Atmospheric Sciences at the University of Illinois for computing assistance, Rachel Humphrey of the Center for Severe Weather Research for help in obtaining the data, and Maxwell Smith and Tim Cermak for their help with graphics. Financial support from the Department of Atmospheric Sciences at the University of Illinois at Urbana-Champaign is also acknowledged.

REFERENCES

Atkins, N. T., A. McGee, R. Ducharme, R. M. Wakimoto, and J. Wurman, 2012: The LaGrange tornado during VORTEX2. Part II: Photogrammetric analysis of the tornado combined with dual-Doppler radar data. *Mon. Wea. Rev.*, **140**, 2939–2958.

Barnes, S. L., 1964: A technique for maximizing details in numerical weather map analysis. *J. Appl. Meteor.*, **3**, 396–409.

Beck, J. R., J. L. Schroeder, and J. M. Wurman, 2006: High-resolution dual-Doppler analyses of the 29 May 2001 Kress, Texas, cyclic supercell. *Mon. Wea. Rev.*, **134**, 3125–3148.

Doviak, R. J., and D. S. Zrnic, 1993: *Doppler Radar and Weather Observations*. Dover, 562 pp.

Frame, J., P. Markowski, Y. Richardson, J. Straka, and J. Wurman, 2009: Polarimetric and dual-Doppler radar observations of the Lipscomb County, Texas, supercell thunderstorm on 23 May 2002. *Mon. Wea. Rev.*, **137**, 544–561.

Frame, J., and P. Markowski, 2013: Dynamical influences of anvil shading on simulated supercell thunderstorms. *Mon. Wea. Rev.*, **141**, 2802–2820.

Koch, S. E., M. desJardins, and P. J. Kocin, 1983: An interactive Barnes objective map analysis scheme for use with satellite and conventional data. *J. Climate Appl. Meteor.*, **22**, 1487–1503.

Kosiba, K., J. Wurman, Y. Richardson, P. Markowski, P. Robinson, and J. Marquis, 2013: Genesis of the Goshen County, Wyoming, tornado on 5 June 2009 during VORTEX2. *Mon. Wea. Rev.*, **141**, 1157–1181.

Kumjian, M. R. and A. D. Schenkman, 2008: Interpretation of the "flying eagle" radar signature in supercells. Preprints, *24th Conference on Severe Local Storms*, Amer. Meteor. Soc., Savannah, GA, paper P14.2.

Majcen, M., P. Markowski, Y. Richardson, D. Dowell, J. Wurman, 2008: Multipass objective analyses of Doppler radar data. *J. Atmos. Oceanic Technol.*, **25**, 1845–1858.

Markowski, P. M., J. M. Straka, and E. N. Rasmussen, 2002: Direct surface thermodynamic observations within the rear-flank downdrafts of nontornadic and tornadic supercells. *Mon. Wea. Rev.*, **130**, 1692–1721.

Markowski, P., Y. Richardson, J. Marquis, J. Wurman, K. Kosiba, P. Robinson, D. Dowell, E. Rasmussen, and R. Davies-Jones, 2012: The pretornadic phase of the Goshen County, Wyoming, supercell of 5 June 2009 intercepted by VORTEX2. Part I: Evolution of kinematic and surface thermodynamic fields. *Mon. Wea. Rev.*, **140**, 2887–2915.

Markowski, P., Y. Richardson, J. Marquis, R. Davies-Jones, J. Wurman, K. Kosiba, P. Robinson, E. Rasmussen, and D. Dowell, 2012: The pretornadic phase of the Goshen County, Wyoming, supercell of 5 June 2009 Intercepted by VORTEX2. Part II: Intensification of low-level rotation. *Mon. Wea. Rev.*, **140**, 2916–2938.

Marquis, J. N., Y. P. Richardson, and J. M. Wurman, 2007: Kinematic observations of Misocyclones along boundaries during IHOP. *Mon. Wea. Rev.*, **135**, 1749–1768.

Marquis, J., Y. Richardson, P. Markowski, D. Dowell, and J. Wurman, 2012: Tornado maintenance investigated with high-resolution dual-Doppler and EnKF analysis. *Mon. Wea. Rev.*, **140**, 3–27.

Oye, R., C. Mueller, and S. Smith, 1995: Software for radar data translation, visualization, editing, and interpolation. Preprints, *27th Conf. on Radar Meteorology*, Amer. Meteor. Soc., Vail, CO.

Pauley, P. M., and X. Wu, 1990: The theoretical, discrete, and actual response of the Barnes objective analysis scheme for one- and two-dimensional fields. *Mon. Wea. Rev.*, **118**, 1145–1164.

Rotunno, R. and J. Klemp, 1985: On the rotation and propagation of simulated supercell thunderstorms. *J. Atmos. Sci.*, **42**, 271–292.

Trapp, R. J., 1999: Observations of nontornadic low-level mesocyclones and attendant

tornadogenesis failure during VORTEX. *Mon. Wea. Rev.*, **127**, 1693–1705.

van den Broeke, M. S., J. M. Straka, and E. N. Rasmussen, 2008: Polarimetric radar observations at low levels during tornado life cycles in a small sample of classic Southern Plains supercells. *J. Appl. Meteor. Climatol.*, **47**, 1232–1247.

Wakimoto, R. M., and H. Cai, 2000: Analysis of a nontornadic storm during VORTEX 95. *Mon. Wea. Rev.*, **128**, 565–592.

Wakimoto, R. M., N. T. Atkins, and J. Wurman, 2011: The LaGrange tornado during VORTEX2. Part I: Photogrammetric analysis of the tornado combined with single-Doppler radar data. *Mon. Wea. Rev.*, **139**, 2233–2258.

Wurman, J., D. Dowell, Y. Richardson, P. Markowski, E. Rasmussen, D. Burgess, L. Wicker, and H. B. Bluestein, 2012: The second Verification of the Origins of Rotation in Tornadoes Experiment: VORTEX2. *Bull. Amer. Meteor. Soc.*, **93**, 1147–1170.

Wurman, J., J. Straka, E. Rasmussen, M. Randall, and A. Zahrai, 1997: Design and deployment of a portable, pencil-beam, pulsed, 3-cm Doppler radar. *J. Atmos. Oceanic Technol.*, **14**, 1502–1512.

Yaffe, K., A. Gordon, and J. Frame, 2012: Analysis of surface thermodynamic characteristics within the rear-flank downdraft of the Wichita, Kansas, tornadic supercell of 14 April 2012. Preprints, *26th Conf. on Severe Local Storms*, Amer. Meteor. Soc., Nashville, TN, paper P1.3.